Chapter 5

Discussion of spectroscopy

5.1 Ground and valence states of ClF

5.1.1 Emission from valence states of ClF (measure of concentration)

The ClF spectra in Fig. 4.2 correspond to vibrational progressions ν'' in the electronic ground state according to the spectroscopic evidence. The energy differences ΔG of successive maxima from Tab. 4.1 are shown in Fig. 5.1 versus ν'' in a Birge-Sponer plot and compared with the IR fundamental frequency $\nu_{0\to1}$ from Ref. [162]. The ΔG values follow the linear regression within the experimental uncertainty given by line broadening. The slopes yield values for the anharmonicity $\omega_e x_e$ in Ar and Kr of 5.77 ± 0.3 cm^{-1} and 6.37 ± 0.15 cm^{-1}, respectively. Thus the anharmonicity increases by 9% (Ar) and by 20% (Kr) compared with the gas phase. The assignment of ν'' to the maxima is chosen in order to obtain extrapolated values for $\nu_{0\to1}$ in agreement with the one measured in IR absorption [162]. This results in an assignment of the progression for Ar to $\nu'' = 2 - 10$ whereas for Kr the assignment is shifted by one to $\nu'' = 1 - 9$. From the linear regression the harmonic frequencies ω_e for the electronic ground state are derived and compared with the gas phase values in Tab. 5.1.

The fundamental frequencies $\nu_{0\to1}$ show the typical red shift in the matrix [128, 196–199]. For ClF in Ar the shift of $\nu_{0\to1}$ is small and less than 0.5% [162] which is consistent with the present data within the experimental error. The value for the matrix shift derived for Kr in this work is larger (1.2%) and agrees once more with Ref. [162]. The main source for the shift is the higher anharmonicity in the matrix. This increase of the anharmonicity of matrix-isolated ClF compared
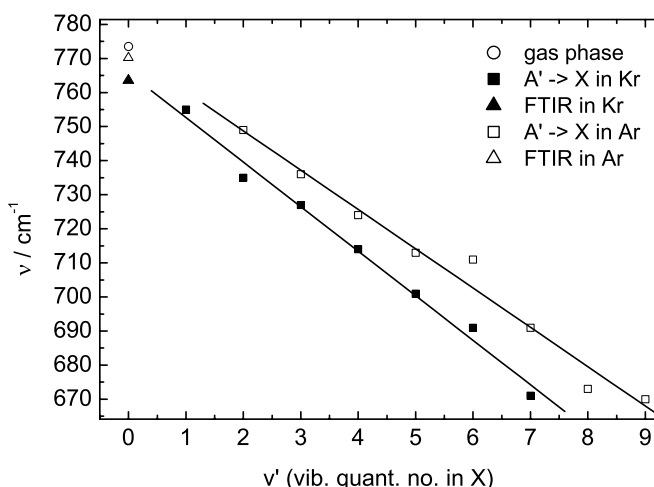

Figure 5.1: Birge-Sponer plot for the $A' \to X$ transition of ClF in Ar (solid squares) and Kr (open squares). The solid lines are linear regressions to the experimental data. Solid and open triangles indicate the frequencies [162] of the vibrational transition $0 \to 1$ of ^{35}ClF for Ar and Kr, respectively. The open circle is the corresponding gas-phase value.

Parameter	gas phase	Ar matrix		Kr matrix		Units
	Ref. [157]	Ref. [162]	this work	Ref. [162]	this work	
$\omega_e(X)$	783.2 ± 0.3		783.5 ± 2.5		777.2 ± 1.5	cm^{-1}
$\omega_e x_e(X)$	5.3 ± 0.1^b		5.77 ± 0.3		6.37 ± 0.15	cm^{-1}
$\nu_{0 \rightarrow 1}(^{35}ClF)$	773.8	770.2	771.8 ± 2.5	763.6	764.5 ± 2	cm^{-1}
$\nu_{0 \rightarrow 1}(^{37}ClF)$	766.6	762.7		756.5		cm^{-1}
$T_e(A')$	18257^a		18111.8 ± 7		17269.1 ± 3.5	cm^{-1}
$T_e(D')_{abs}$	55253		50750 ± 400			cm^{-1}
$T_e(D')_{em}$	55253		45270 ± 20			cm^{-1}

a) Ref. [145], b) A value of $\omega_e x_e = 4.8$ cm^{-1} is obtained if higher order terms are included.

Table 5.1: Potential parameters for ClF in the gas phase and in rare gas matrices. The gas phase values are for ^{35}ClF unless stated otherwise. Line broadening effects cover the isotope splitting in electronic transitions.

to the gas phase indicates that the cage atoms do not lead to a stiffening of the potential around the equilibrium distance but instead the polarizability weakens the $Cl - F$ binding, especially in Kr. A stiffening as observed in the case of I_2 (cf. chapter 7.1.2 and ref. [200]) will occur for larger $Cl - F$ elongations (not accessed by the $A' \rightarrow X$ emission), where the barrier induced by the repulsive forces from the cage atoms comes into play.

The linewidths of the individual vibrational transitions are given in Table 4.1. The average linewidths of the bands are $H = 250$ cm^{-1} for argon and $H = 306$ cm^{-1} for krypton and there is no trend with increasing vibrational number. A similar linewidth of 260 cm^{-1} has been found for IF isolated in Ar [198].

The electronic energy T_e of the upper, emitting electronic state is obtained from the measured peak positions and the linear regression in Fig. 5.1. The emitting state is assigned to $A'\,(^3\Pi_2)$, because of the extremely long radiative lifetime of $\tau = 141 \pm 6$ ms. It fits well into the trend of other halogens and interhalogens [198], which reflects the fact that selection rules become stricter for lighter molecules. All $^3\Pi \rightarrow X\,(^1\Sigma_0)$ transitions are spin forbidden and the $A'\,(^3\Pi_2) \rightarrow X$ transition is additionally forbidden by the angular momentum selection rule $\Delta\Omega = 0, \pm 1$. The lifetimes for transitions from $A\,(^3\Pi_1)$ and $B\,(^3\Pi_0)$ are known to be in the μs range for other interhalogens [198]. Having assigned the emitting state to A', its electronic energy $T_e(A')$ is calculated (cf. Tab. 5.1) using the known harmonic frequency of the A' state in the gas phase $\omega_e(A') = 363.5$ cm^{-1} [145]. The rather small red shift of the A' state from the gas phase to the Ar solid is typical for valence states (1-2%) [74, 79]. The increase of the red shift from 150 cm^{-1} in Ar to 990 cm^{-1} in Kr reflects the larger inductive and dispersive forces [129] discussed in chapter 2.2. The shift of 5.4% in Kr is large for a valence state. Shifts of the same order were observed for some fluorine-containing diatomics [74] e.g. KrF [193] and XeF [201] isolated in Ar.

5.1.2 Absorption (pump pulse)

The absorption of ClF in matrices could not be measured and the reported gas phase values (Fig. 2.12) have to be used. Since the shift of the $A' \rightarrow X$ emission is only 1% in Ar, a negligible shift is expected for the valence states in absorption, and for all results in this thesis unshifted valence states are taken. A value for the absorption cross section at 308 nm is interpolated from the data in Ref. [150]. From ref. [149] a value of 3.9×10^{-21} cm^2 is obtained, which is slightly higher than the value of 3.0×10^{-21} cm^{-2}. The intermediate value of $\sigma_{308} = 3.5 \times 10^{-21}$ cm^2, which should be accurate to within $\pm 25\%$, is listed in Tab. 5.4.

To check the consistency of the absorption data from the literature with the calculated potential surfaces, the ground state wave function is projected in Fig. 5.2 onto the repulsive limbs of the two
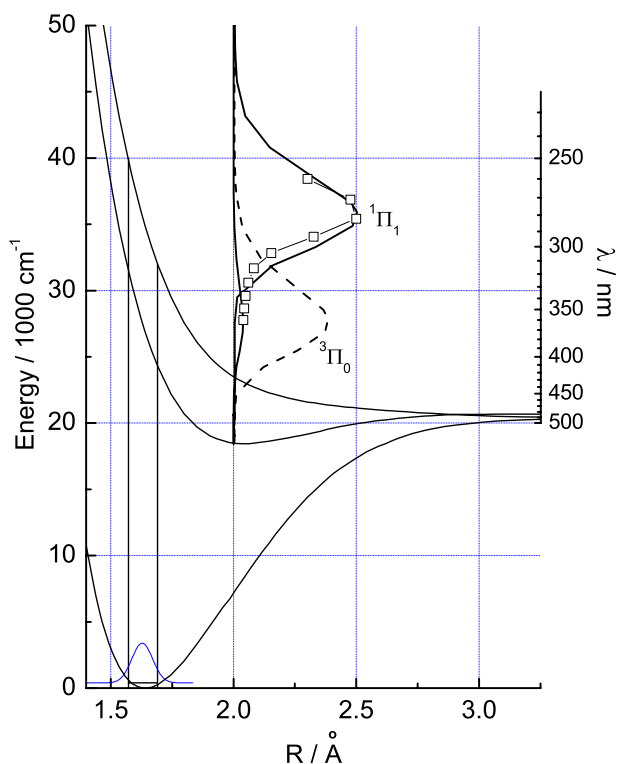
Figure 5.2: Absorption bands calculated from the projection of the ground state Gaussian onto the repulsive limbs of the $^1\Pi$ (solid) and $^3\Pi_0$ state (dashed). The open squares reproduce the absorption of ClF measured in ref. [150].

valence states [121] allowed by the $\Delta\Omega$ selection rule. Obviously, the $^1\Pi$ state gives rise to the strong absorption observed in ref. [150] that is reproduced in Fig. 5.2 as open squares. The transition to $B(^3\Pi_0)$ is spin-forbidden and very weak. The shoulder in the poor experimental absorption spectra may be due to the weak absorption to the B state. The long known and well resolved discrete B state spectra in the bound region [156] and the OODR experiments [133] demonstrate that the absorption in the Franck-Condon region is strong enough to record pump-probe spectra. No published values for the absorption cross section at 387 nm are available. An approximate relative intensity of the B state vs. $^1\Pi_1$ absorption is derived from the intensity ratios of the $A' \rightarrow X$ fluorescence bands of ClF and Cl_2 within the same spectra, upon irradiation at 308 nm (Fig. 4.2b) and 387 nm (Fig. 4.2a). The known absorption for Cl_2 [153] is thus used for calibration. The ratio of the absorption cross sections of ClF of $\sigma_{308}/\sigma_{387} \approx 8$ is obtained with a rather large uncertainty and the calculated B state absorption in Fig. 5.2 is scaled accordingly (cf. Tab. 5.4: $\sigma_{387} \approx 4.5 \times 10^{-22}$ cm^2).

5.2 Ionic states of ClF, Cl_2 and excimers

5.2.1 Emission from ionic states of Cl^+F^- (LIF)

The three dominant emission bands in Fig. 4.5 were already assigned with spectroscopic arguments to allowed transitions from the vibrationally relaxed ionic state $D'\,(^3\Pi_2)$ to valence states. From the large manifold of 16 valence states only $A'(1^3\Pi_2)$, the $2(^3\Pi_2)$ and the $2\,(^3\Delta_2)$ give rise transitions allowed by the selection rules $\Delta S = 0$ and $\Delta\Omega = 0$. Therefore the spectrum in Fig. 4.5 between 21,000 cm^{-1} and 27,000 cm^{-1} is approximated by three Gaussians. A fourth Gaussian takes into account the wing around 20,000 cm^{-1} which does not bleach with irradiation dose as the others do and is thus of different and yet unidentified origin. It will not be considered in this thesis.

The fit of the experimental spectrum in Fig. 4.5 was done without using spectroscopic information. The energy and equilibrium distance of the emitting ionic state is derived from the fitted peaks. The

Peak	Position	Width	Assignment
1	25474 ± 14	1536 ± 20	$D' \rightarrow A'\,^3\Pi_2$
2	23869 ± 6	1521 ± 21	$D' \rightarrow 2\,(^3\Pi_2)$
3	22322 ± 19	1539 ± 55	$D' \rightarrow 2\,(^3\Delta_2)$
4	20699 ± 57	2256 ± 74	unknown

Table 5.2: Positions and widths (fwhm) for the D' emission of ClF in Ar onto valence states obtained by fitting the measured fluorescence band by four Gaussian peaks. The assignment is discussed in the text. All values are in units of cm^{-1}.

fit results in three bands with equal widths of 1530 cm^{-1} and an approximately equal spacing of 1575 cm^{-1} (Tab. 5.2). In calculated potential energy curves for gas phase ClF [121] the bond distance $R \approx 5.1$ a$_0$ produces the calculated spacings between the three valence states $A'(1^3\Pi_2)$, $2(^3\Pi_2)$, and $2\left(^3\Delta_2\right)$. Since the population in the ionic state has relaxed into the vibrational ground state of the lowest ionic state, D', this value of R gives the equilibrium position R_{eq} of the D' state in the matrix. It is significantly expanded compared to the gas phase value $R_{eq} = 4.85$ a$_0$, indicating the strong solvation of the ionic states. According to the potentials [121], a smaller value for R would result in a larger spacing of the three bands than the one observed. The spacing of the valence states is not expected to be changed significantly in the matrix.

Using the measured transition energies and the gas phase valence band energies, the electronic energy of the emitting state is $T_e\left(D'\right)_{em} = 45270 \pm 20$ cm^{-1}. This yields a red shift of about 10,000 cm^{-1} compared to the gas phase. Such a strong shift both in energy and equilibrium position is large but not exceptional, because it reflects the energy gain in solvation of the ionic dipole [202] and the Franck-Condon factors in the configuration coordinate after rearrangement of the Ar-lattice (Fig. 2.7). A comparable shift of 11200 cm^{-1} has been observed for Cl_2/Ar [134]. Larger molecules undergo weaker shifts (2100 cm^{-1} for IBr/Ar [196] and 2900 cm^{-1} for I_2/Ar [79]), which may be explained by the semi-empirical formula eq. 2.6 for the solvation-shift.

The onset of two-photon excitation (see chapter 4.2.3) yields a value of $T_e\left(D'\right)_{abs} = 50750$ cm^{-1} in absorption which represents a red shift of 4500 cm^{-1} compared to the gas phase [121] and is due to electronic polarization (chapter 2.2.3). The value is comparable to shifts in absorption from valence to ionic states in other molecules [130]. The further red shift of 5500 cm^{-1} from $T_e\left(D'\right)_{abs}$ to the value in emission $T_e\left(D'\right)_{em}$ corresponds to a Stokes shift E_s caused by the lattice rearrangement. The Stokes shift E_s and the line width H are used in a configuration coordinate model for the rearrangement to give an approximation for the Huang-Rhys phonon coupling constant S (chapter 2.2.4). From the experimental values for E_s, a large coupling constant $S = 40$ is derived, assuming a typical phonon energy $\hbar\omega_p = 69$ cm^{-1} in argon crystals. In this approximation, the electron-phonon coupling accounts for a linewidth of $H = 1030$ cm^{-1}, which is smaller than the observed one. Note however, that the measured linewidth is expected to be broader, since the projection of the wave function from the vibrational ground state of D' onto the valence states yields a bandwidth of 500 cm^{-1}. A Gaussian superposition accounts for a width of 1145 cm^{-1} which is still too small. Higher than linear order of coupling can explain the difference, but since the linewidth in absorption is not available, further improvement is not pursued. The value of $S = 40$ indicates a strong coupling corresponding to a significant lattice rearrangement and an average of generated phonons on the order of 40 in an absorption or emission event. The phonon coupling dominates the line broadening, leading to equal widths in all three transitions.
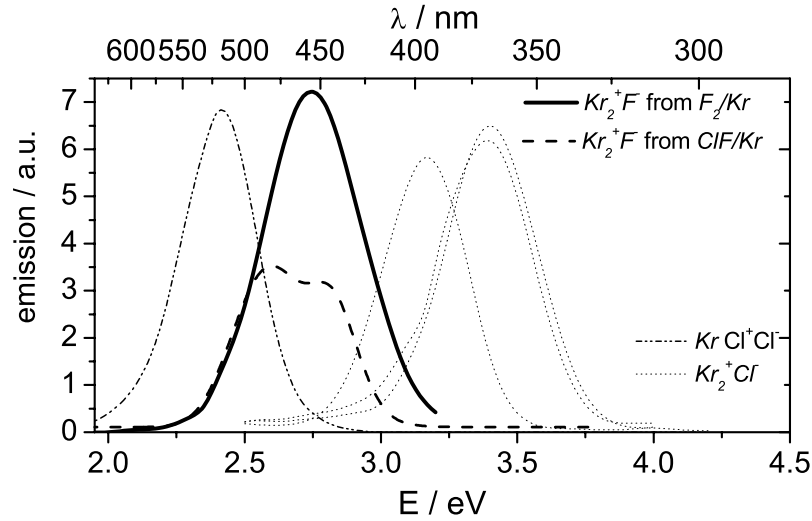
Figure 5.3: $Kr_2^+F^-$ emission measured in this thesis by dissociating ClF (thick dash) compared to the same emission after F_2 dissociation in Kr (thick solid [82, 193]) and to the emissions from $KrCl$ (three dashed curves for different sites [194]) and $KrCl_2^-$ (dash-dot [194]).

5.2.2   Identification of $Kr_2^+F^-$ emission (LIF)

The $Kr_2^+F^-$ emission recorded in this thesis by dissociation of ClF in Kr at $\lambda_{diss} = 387$ nm and probing the F fragments with $\lambda_{probe} = 270$ nm is reproduced in Fig. 5.3 as a thick dashed line (Gaussian fit from Fig. 4.6). It is compared to the same emission for F_2 in Kr [82] (thick solid line), to Cl^+Cl^-/Kr (dash-dotted) and to Cl atoms in different lattice sites (three dotted curves) [194]. Only the $Kr_2^+F^-$ emission after F_2 dissociation is comparable. Since the emission grows with sample irradiation, the nearby $KrCl_2$ emission cannot be a candidate.

As a check, two $Kr_2^+F^-$ emission bands taken from literature were fitted with the same Gaussian functions in Fig. 5.4, with their amplitudes and widths as the only adjustable parameters. Good agreement with the spectrum reported by Bressler [82, 193] (open squares, excited with 260 nm) is obtained, when the weight of the Gaussian at 441 nm is approximately doubled. For the spectrum recorded in Apkarian's group [54] (open circles, excited at 248 nm), it must be almost quadrupled. Until now, the broad spectra were interpreted as the vertical transition to the repulsive $Kr - Kr$ surface [54, 69]. As the emission observed in this thesis clearly consists of two bands and the spectra reported for different excitation wavelengths are shifted with respect to each other, an explanation involving two different lattice sites, which lead to different fluorescence spectra, seems natural.

The two bands most probably originate from different positions of the emitting $Kr_2^+F^-$ exciplex in the Kr lattice. A longer emission wavelength is expected in a tight geometry and the 480 nm band is therefore assigned to fluorescence on interstitial sites, i.e. Kr^+F^- is excited while F is on an interstitial site. During the formation of the $Kr_2^+F^-$ exciplex the $Kr - Kr$ bond is contracted by 44% [47] and this complex fluoresces in the tight geometry. The 441 nm band is favored by excitation of substitutionally isolated F atoms. After formation of the $Kr_2^+F^-$ exciplex, the geometry is less constrained due to the vacancy of the substitutional site. This explains why the 441 nm band dominates in F_2 doped samples, since F atoms may occupy both substitutional and interstitial sites. Dissociation of ClF, in contrast, produces mostly interstitial F fragments, because the substitutional
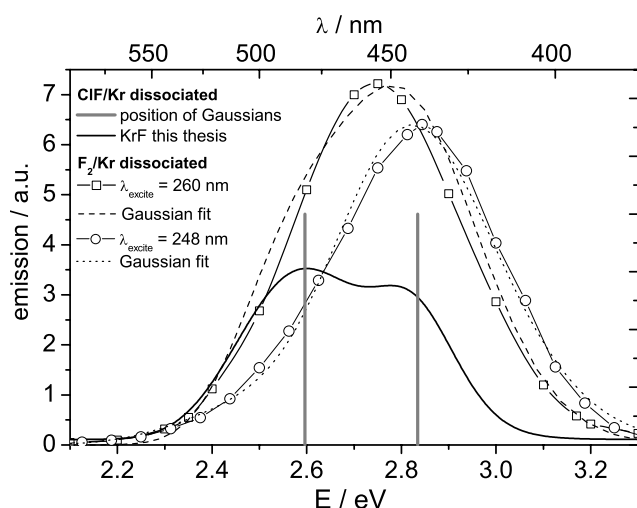
Figure 5.4: The Gaussian fit to the $Kr_2^+F^-$ emission (thick dashed) measured in this thesis after ClF dissociation and excitation at 270 nm is reproduced from Fig. 4.6a. The vertical sticks indicate the position of the two Gaussian functions. The symbols reproduce the $Kr_2^+F^-$ emission after F_2 dissociation in Kr and excitation with 260 nm (open squares, ref. [82, 193]) or 248 nm (open circles, ref. [54]). The dashed and dotted lines are fits with the two Gaussians at the indicated positions.

sites are occupied by the immobile Cl. Both bands can be excited with pulses ranging from 278 nm to 248 nm, but the shorter wavelengths preferentially excite the 441 nm fluorescence band (cf. Fig. 5.4).

An emission from Cl^+F^-/Kr could not be observed. It is expected to be shifted to the red with respect to the emission in Ar at 420 nm. This emission would then overlap with the emission from $Kr_2^+F^-$. However, the observed emission grows with irradiation (cf. chapter 4.3.3), implying that it cannot be due to Cl^+F^-/Kr, which should be bleached. Probably the Cl^+F^-/Kr is quenched by nonradiative recombination[1].

5.2.3   Excimer absorption of KrF (probe pulse)

When ClF is dissociated in the matrix, the F and Cl radicals are bound by approximately 100 cm^{-1} due to van-der-Waals interaction with the surrounding Ar and Kr matrix atoms. The van-der-Waals minima of the gas phase potentials of Cl and F to the rare gases are collected in Tab. 5.3 and compared to the nearest neighbor distance (substitutional site) and to the distance from the center of the octahedral O_h site to the rare gas atoms in an undistorted lattice.

For a concise discussion consider Fig. 5.5. The absorption of KrF in Ar matrices shows a sharp onset at 265 nm and a well resolved vibrational progression, indicating absorptions to different vibrational levels in the ionic Kr^+F^- state, $v' \to v''$ from $0 \to 0$ to $0 \to 9$ [82]. The main point is that the transition to the zeroth vibrational level in Kr^+F^- is observed with the highest intensity. This can be explained by the fact that in an octahedral O_h site in Ar with one Kr atom, the $Kr - F$ distance will be approx. 0.266 nm, which is so close to the minimum $R_e = 0.25$ nm of the Kr^+F^- potential, that the overlap of the vibrational ground state wave functions in the valence and ionic state is very large. The same configuration in Ne matrix leads to a $Kr - F$ bond confined to a distance of only 0.224 nm, and the $0 \to 0$ transition has only a weak intensity, whereas the maximum occurs around $0 \to 9$ [82]. Again, this can be explained by a projection onto the repulsive wall of the Kr^+F^- potential at 0.224 nm.

In contrast, the absorption spectrum of KrF in Kr matrix (Fig. 4.9) lacks vibrational structure. In the center of the octahedral site (cf. Fig. 2.5) of an undistorted Kr matrix, the F atom has a distance of 0.286 nm to six Kr atoms. This distance happens to be exactly the van-der-Waals bond

---

[1]Note that the difference in ionization potentials $E^+(Kr) - E^+(Cl) = 1eV$ is on the order of the binding energy of $Kr_2^+F^-$ with respect to Kr^+F^- of 0.66 eV [47] and the binding energy of Kr_2^+ of 1.15 eV [48].
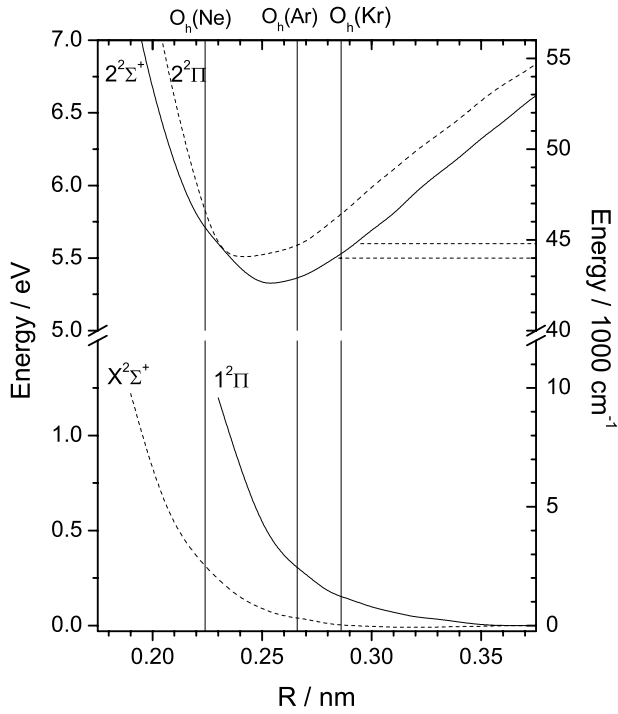
Figure 5.5: KrF potential calculated by Dunning and Hay [51]. Vertical lines indicate the $Kr - F$ distance in an interstitial O_h site of Ne, Ar and Kr in an undistorted lattice. The distance in Kr coincides with the van-der-Waals distance of $Kr - F$. The dashed horizontal lines display the width of the sharp absorption at $\lambda = 275$ nm of KrF at 4 K (Fig. 4.9).

Matrix	notation	Ne	Ar	Kr
van der Waals to F [57]	R_{vdW} / nm		0.31	0.285
min of Rg^+F^- [51]	$R_{\min \Delta V}$ / nm	0.201	0.245	0.25
van der Waals to Cl [56]	R_{vdW} / nm		0.388	0.395
nearest neighbor [119]	R_{nn} / nm	0.316	0.376	0.404
octahedral site [119]	R_{os} / nm	0.224	0.266	0.286

Table 5.3: Bond lengths of van-der-Waals RgX molecules and lattice parameters.

length of KrF. Therefore, the F atom will be in the center of the O_h site, and this highly symmetrical configuration gives rise to the sharp absorption at 275 nm [88] at 4K (cf. Fig. 4.9). Upon irradiation more and more F atoms are trapped in the O_h site. At higher temperatures, vibrations of the lattice and of the F fragment within the cage destroy the symmetry, and since the F atom has various distances to the nearest Kr atoms the absorption broadens. For temperatures higher than 15 K, F becomes thermally mobile in the matrix and occupies various sites. This changes the absorption band to the one observed by Bressler, Andrews and in this thesis at high T (Fig. 4.9). The vibrational structure is missing, since different sites inhomogeneously broaden the peaks.

At low temperatures, $\lambda_{probe} = 278$ nm does not lead to recombination of ClF or F_2 by radiative dissociation of $Kr_2^+F^-$, whereas $\lambda_{probe} < 270$ nm does. Bressler observes that the sharp 275 nm absorption grows with photon flux at 275 nm, while it decays when the sample is irradiated with shorter wavelengths. Also the relative weight of the emissions at 441 and 480 nm depends on the excitation wavelength (Fig. 5.4). These observations together support the following hypothesis: the shorter λ_{probe} is, the higher the energy in the ionic manifold will be, and the possibilities for a geometric rearrangement within the ionic state increases. Then the fluorescence may occur in a geometry favoring recombination. If λ_{probe} is kept low, the fluorescence must occur in such a way as to retain F inside the O_h site. The dependence of the relative weight of the two bands on excitation, discussed in the previous chapter, is consistent with this interpretation.

The following implications of the spectroscopy in Kr matrix for the pump-probe experiments with the KrF excimer as the probed species can be inferred. The fluorescence bands at 441 and 481 nm are indicative of KrF formation. If a wavelength $\lambda_{probe} < 270$ nm is used, the F atoms, which have not reached the O_h site, will contribute little to the signal. Warm matrices enforce thermal recombination but at the same time greatly reduce the static fluorescence intensity induced by $\lambda_{probe} \approx 275$ nm.

The interpretation of both the spectroscopic results and the interpretation of pump-probe spectra will greatly profit from a detailed theoretical investigation of the ionic species. The calculation of precise ion-pair states by the DIIS method is a complicated task and has not been accomplished for F in rare gases, but is investigated in the groups of Prof. Gerber and Prof. Manz.

5.3   Potential energy surface for ClF in Ar matrix

A.B. Alekseyev kindly provided us with the numerical data for the potentials of ClF in the gas phase [121]. The calculation of DIM potentials for ClF in Ar are in progress[2]. Throughout this thesis gas phase potentials are used, with the ion-pair states shifted according to the results from chapter 4.2.3 which are collected in Tab. 5.1.

5.3.1   Difference potentials for ClF

Difference potentials ΔV are needed for the evaluation of the pump-probe spectra. Fig. 5.6c shows the bound triplet states $^3\Pi$, the first excited singlet $^1\Pi$ and an exemplary repulsive triplet state. The thick line emphasizes the $B(^3\Pi_0)$ state, which is excited in most of the pump-probe experiments discussed below. Panel b) displays the shifted difference potentials for all triplet-triplet transitions which obey the propensity rule $\Delta\Omega = 0$. The lowest transition from the singlet state has its minimum around $41000 \, \text{cm}^{-1}$, above the scale of this plot. The thick lines indicate the $B \rightarrow E$ (solid) and $B \rightarrow f$ (dash-dot) transitions. The transitions from other bound states have similar difference potentials. The transitions from the repulsive triplet state are plotted as dashed lines. They have not been observed in this thesis, as the longest probe wavelength that resulted in a pump-probe signal was 320 nm, and the ionic potentials where shifted to have the $B \rightarrow E$ resonance at this wavelength.

The square of the transition moments for the $B \rightarrow E$ and $B \rightarrow f$ transitions is plotted in the upper panel of Fig. 5.6. The transition to f dominates for short bond distances and probe wavelengths. For bond distances $R > 6 \, \text{a}_0$ the transition moment is negligible, prohibiting probe windows at these large distances. The transition probabilities for the other bound triplet states are similar [158] and the ones for repulsive triplets are weaker [121]. If the repulsive triplets were significantly populated, a pump-probe signal with $\lambda_{probe} > 320$ nm should be observed.

5.3.2   Difference potential of Cl_2

Fig. 5.7a displays the difference potentials for the $B \rightarrow E$ (solid) and $B \rightarrow f$ (dash dot) transitions in Cl_2/Ar, shifted in the same way as for ClF, namely as to match the excitation threshold for the Cl^+Cl^-/Ar emission at 286 nm. Panel b) shows the potential energy curves for the relevant states of Cl_2. The ground state X, the B state (solid) as a representative of the bound triplets, the $^1\Pi$ state (dash) and two states from the repulsive manifold (dotted) are displayed. The E (solid) and the f state (dash dot) are indicated.

5.4   Photochemistry of ClF in Ar and Kr

Cl atoms (and all larger compounds formed by it) are spatially fixed in Ar and Kr matrices. F atoms become thermally mobile at $T = 25$ K in Ar and at $T = 15$ K in Kr [81]. At temperatures below this threshold, they are fixed but can move, if they receive enough kinetic energy in a photodissociation event. These photo-mobilized F atoms travel a certain distance in the crystal until they have lost their

---

[2]PhD thesis by Maike Schröder in the cooperating group of Prof. Manz, Theoretical Chemistry Department
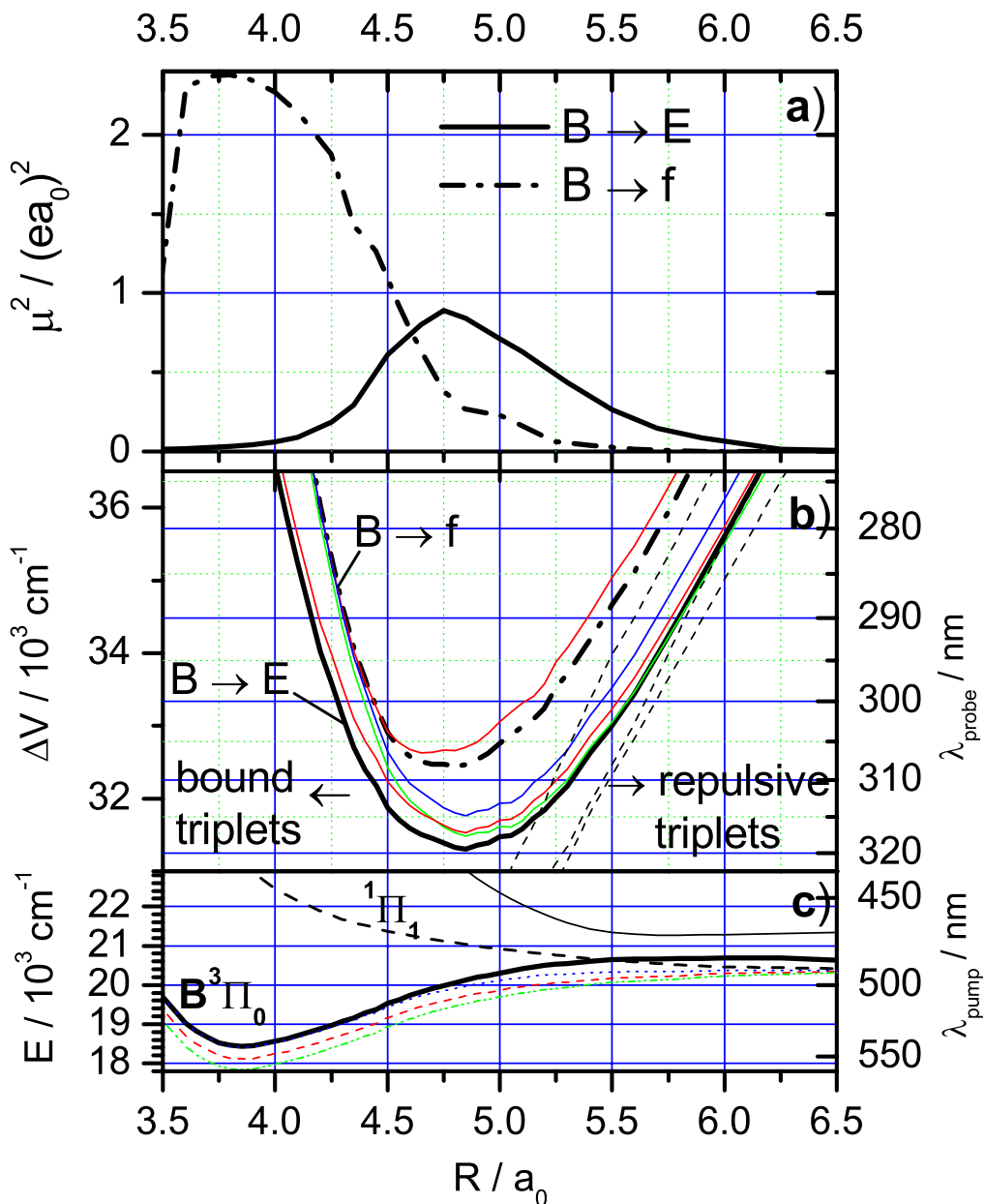
Figure 5.6: Results obtained in the CI calculations for ClF from ref. [121]. a) Square of the transition dipole moment μ^2. The transitions with $\Delta\Omega \neq 0$ have weak dipole moments, and their μ^2 is two orders of magnitude smaller. b) Difference potential ΔV red shifted by 4500 cm^{-1}. The thick solid line corresponds to the $B \rightarrow E$ transition and the thick dash-dotted line to $B \rightarrow f$. c) Potential energies for some valence states.
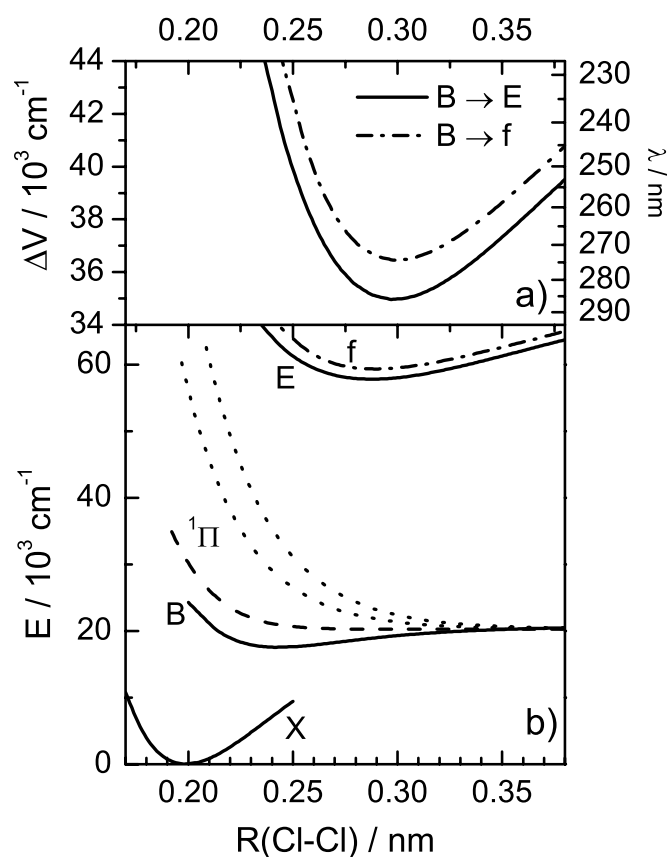
Figure 5.7: a) Difference potential for Cl_2 shifted by 3760 cm^{-1} for the $B \rightarrow E$ (solid) and $B \rightarrow f$ transition (dash dot). b) Unshifted potential surfaces of Cl_2. Ground state X, B (solid), $^1\Pi$ (dash) and two repulsive triplet states (dotted). At higher energies E (solid) and f (dash dot).

energy. Then they are trapped, either in a rare gas cage or by a center with which they react. In Ar they travel on average about 2.1 nm upon photoexcitation with 3 eV excess energy [203]. Traps for F fragments are ClF itself, Cl and F from previous dissociation events and also molecular products like F_2, ClF_2 and ClF_3 formed by previous fragmentations. At the excitation wavelength of 308 nm the products ClF_2 and F_2 are known to absorb much more strongly, approximately by a factor of 4, than ClF itself [152, 173]. Nongeminate recombination should become rare at concentrations as low as 1 : 100,000, since the average distance traveled by photomobilized F fragments has been shown to be around 8-9 lattice constants [203]. The mean distance between two ClF molecules deposited at a concentration of 1 : 100,000 is 46 lattice constants.

The objective of this thesis is to investigate the ultrafast photodynamics in the primary dissociation event by fs-pump-probe spectroscopy. A more detailed study of the static photochemical experiments is deferred.

5.4.1 Dissociation quantum efficiency

ClF/Ar

Here the evaluation will restricted to exponential fits, which should indicate within a factor of two the dissociation efficiency and its dependence on temperature and wavelength. The dissociation efficiencies ϕ_d are calculated from $\sigma\phi_d$ derived in chapter 4.3. The absorption cross sections σ are taken from Tab 5.4. This yields dissociation efficiencies at 308 nm in argon of $\phi_{d,308} = 4.4\%$ at 5 K and 5.0% at 19 K using the lowest concentration (see Table 5.4). The dissociation quantum yield of $\phi_{d,387} \approx 4.8\%$ for excitation at 387 nm measured at 19 K has to be used with care, since the large uncertainty in the value for σ_{387} enters.

		F_2			ClF				units
atom 1	m	19			19				amu
atom 2	M	19			35				amu
diss. energy	D_0	12820			20930				cm^{-1}
excitation wavel.	λ	360	450		308		387		nm
photon energy	$h\nu$	27780	22222		32468		25840		cm^{-1}
energy of F	E_{kin}	7430	4650		7370		3070		cm^{-1}
absorpt. x-section	σ	5.16 [a]	0.23 [a]		3.5		0.44		10^{-21}cm^2
diss. x-section	$\sigma\phi_d$	1.86	0.081	0.028	0.15 0.18	1.8	0.021	0.22	10^{-21}cm^2
diss. quant. yield	ϕ_d	36 [b]	35 [c]	12 [c]	4.4 5.0	50	4.8	50	%
temperature	T	12	4.5	12	5 19	28	19	20	K
host		Ar	Kr		Ar	Kr	Ar	Kr	

a) Ref. [152], b) Ref. [81], c) Ref. [53]

Table 5.4: Summary of dissociation efficiencies for ClF determined in this work by bleaching of the A emission. Earlier results for F$_2$ are included for comparison.

The values for the dissociation efficiencies of $4.4 - 5\%$ reported here are low considering the excess energy of 0.9 eV for the F fragment and the fact that excitation at 387 nm with a lower excess energy of 0.4 eV still leads to photodissociation. One has to keep in mind, though, that these values for the efficiency for permanent dissociation are determined by the cage exit probability *minus* the probability for geminate and nongeminate recombination.

The results for ClF are compared to the dissociation efficiencies obtained for F_2 [53, 81] at the same kinetic energies E_{kin} of the F fragments in Tab. 5.4. The excess energy E_e given by the difference between the photon energy $h\nu$ and the dissociation energy D_0 is shared among the fragments according to momentum conservation. This leads to a kinetic energy E_{kin} of the lighter F fragment of $E_{kin} = (h\nu - D_0) \times M/(M + m)$ with $m = 19$ amu for F and $M = 35$ amu for Cl. The results show the expected trend of decreasing dissociation probability going from 5% to 4.8% when lowering the kinetic energy of the F fragment from 0.91 eV (7370 cm^{-1}) to 0.38 eV (3070 cm^{-1}). However, one might expect a larger change as in the case of F_2 [53, 81] (cf. Tab. 5.4). The ClF results for ϕ_d are significantly lower than those reported in [53, 81] for F_2 dissociation. A possible explanation may be found in the orientation of the F orbital. Calculations of the transmission coefficient of an F atom through the triangular window shown in Fig. 2.5c showed [68] that the barrier for an F atom with the singly occupied F orbital aligned parallel to the direction of motion is 2.1 eV, with a saddle point in the center of the triangle. For the P-orbital orientation perpendicular to the motion, the saddle point is in the line connecting two nearest neighbor Ar atoms with a barrier height of only 0.7 eV. For symmetry reasons, and from the considerations on the molecular orbitals in Fig. 2.14, it is evident that a dissociating F_2 molecule will have parallel and perpendicular P-orbital orientation on both F fragments with equal probability. For ClF, the singly occupied P-orbital on the F fragment is always aligned with the direction of motion and thus it experiences the higher barrier, if the orbital is not tilted on the timescale of dissociation. Simulations on the orbital orientation of F atoms in matrices suggest [70] that the timescale of orbital alignment will be on the order 60 fs. This point deserves further experimental and theoretical attention.

Clearly, detailed studies of the reaction mechanism and the dissociation efficiency are required to elucidate pathways and cage exit probabilities. However, even the preliminary results given here have important implications. Since the kinetic energy of the F fragment is lower in the case of excitation of ClF at 387 nm than for F_2 at 450 nm the observation of permanent cage exit sets a new upper bound for the barrier height for F in Ar of 0.4 eV.

ClF/Kr

The yields for Kr are calculated in the same way (Tab. 5.4). They are on the order of 50% in warm matrices and at relatively high concentrations of $1 : 5000$. The mobility of F fragments is very high and repeated re-excitation can expel the F fragments from the laser focus.

In this system not only the bleaching of the educts ClF, but also the accumulation of the products can be measured by inducing the KrF excimer transition and measuring the $Kr_2^+ F^-$ emission. If the early rise in Fig. 4.14a is fitted with an exponential growth curve, as it was done in the Apkarian group [88] for the F_2 dissociation in Kr, a dissociation efficiency beyond 100% is calculated. This result is unphysical. It can be explained in terms of a saturation value induced by secondary processes and back reaction, i.e. the concentration of ClF does not decrease to zero. This is consistent with the finding of nonexponential decay or background in the ClF bleaching experiments. Obviously, the cage exit probability and mobility of F fragments in Kr is very high. In the future it will be helpful to detect the ClF educt and the KrF product of the dissociation simultaneously in order to find quantitative solutions of the rate equations. This can be done for example by exciting ClF with $\lambda_{diss} = 387$ nm, which dissociates ClF and induces the $A' \rightarrow X$ of the remaining ClF educts. A weak probe laser at $\lambda_{probe} = 270$ nm then records the KrF products. Experiments employing these pulses were reported in chapter 4.3.3. However, the $A' \rightarrow X$ emission was not monitored there, as this study aimed at preparing the femtosecond experiments. The results are discussed in the following chapter.

### 5.4.2 Control of F motion: Shuttling F from Cl to Kr

Fig. 4.14 demonstrates that there are two ways to control the concentration of F fragments with laser pulses. The dissociation laser $\lambda_{diss} = 387$ nm can drive the ClF dissociation to completion and the probe laser $\lambda_{probe} = 270$ nm induces recombination of the ClF fragments, because the fluorescence of $Kr_2^+ F^-$ mobilizes the F atoms. In other words, the F atoms can be shuttled from Kr to Cl much in the same way as was previously demonstrated for multiply doped Ar matrices, where F atoms are shuttled from Xe to Kr and back [81].

A second, more sophisticated way to shift the equilibrium uses a sequence of pulses on the fs timescale. This is demonstrated in Fig. 4.14b between 400 and 580 s. After the dissociation with λ_{diss}, the F fragments are not in thermal equilibrium for several ps, i.e. they move within the Kr crystal. The detection efficiency at λ_{probe} for these hot F atoms is enlarged and therefore the observed signal is higher for the sequence B, where $\lambda_{probe} = 270$ nm comes 100 fs after $\lambda_{diss} = 387$ nm. In sequence A (λ_{diss} 1 ps after λ_{probe}), almost 1 ms passes between λ_{diss} and λ_{probe}, because the repetition rate of the laser is 1 kHz, and after this time all F fragments have thermalized in the Kr lattice. The signal alternates from equilibrium A to B in a stepwise manner, when the time delay is changed accordingly. A closer look at the step function shows that after the step up there is some additional rise, and after the step down there is a decay, indicating that in addition to the altered detection efficiency, also the equilibrium concentration changes. Consider the decay from B to A between 400 and 420 s in Fig. 4.14b. λ_{probe} comes 1 ms after λ_{diss} during this time and thus only thermally equilibrated F fragments are probed. The decay must originate from a decay of the F concentration. The reason for the higher F concentration produced by the sequence B is that the recombination of ClF induced by λ_{probe} is completed before the dissociation with λ_{diss} and thus there are more ClF molecules to dissociate.

Rate equations

This chapter gives a description of the photochemical equilibria by rate equations, that may become important in future investigations. This thesis focuses on the fs-pump-probe experiments and here

only the shape of the observed rise and decay functions of Fig. 4.14 shall be explained. The full rate diagram

$$ClF + Kr \overset{k_1}{\underset{k_2}{\rightleftharpoons}} Cl + KrF \overset{k_3}{\rightarrow} Cl + Kr + XF$$
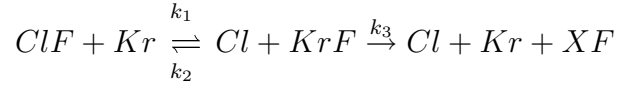
can be described by the a system of differential equations for the concentrations N_i

$$
\begin{aligned}
dN_1 &= -k_1 N_1 + k_2 N_2 \\
dN_2 &= +k_1 N_1 - k_2 N_2 - k_3 N_2 \\
dN_3 &= k_3 N_2
\end{aligned}
$$

with $N_1 = N_{ClF}$, $N_2 = N_{KrF}$, $N_3 = N_{XF}$, and XF denotes any of the species such as $Cl_2 F$, ClF_2 etc., or F atoms that have left the laser focus.

The solution for the KrF concentration, which is measured in the experiment by λ_{probe}, is[3] $N_2(t) = C_0 + C_1 \exp((-\kappa_1 - \kappa_2)t) + C_2 \exp((-\kappa_1 + \kappa_2)t)$. This function describes the fast initial rise and slow decay of the entire signal, i.e. when pulse sequences are not changed.

In order to determine the individual rates from the experiment, the rate k_3 can be neglected (at least for weak pulses as used for figure 4.14a). The solution for this reduced system is $N_2(t) = N_{eq} + (N_0 - N_{eq}) \exp(-(k_1 + k_2)t)$, which describes all rise- and decay functions in Fig. 4.14. N_0 is the starting value and N_{eq} is the equilibrium value. Since $\lambda_{probe} = 270$ nm dissociates ClF and also drives the recombination, the rate constants must be rewritten as $k_1 = k_{387} + k_{270}$ and $k_2 = k_{probe}$. The rise and decay rates are the sum of the three rates k_{387}, k_{270} and k_{probe}. Three equations are needed to obtain the rates. Two are determined by the rates for the rise $k_r = k_{387} + k_{270} + k_{probe}$ and decay $k = k_{270} + k_{probe}$. A third equation can be derived from the steady state concentration N_2^{eq} and the total number of available F fragments N_{allF}, which is measured in the highest spike in Fig. 4.14, when λ_{diss} has driven the ClF dissociation to completion: $\frac{k_{270} + k_{387}}{k_{probe}} = \frac{N_2^{eq}}{N_{allF} - N_2^{eq}}$.

---

[3]using the definitions $\kappa_1 = \frac{1}{2}k_1 + \frac{1}{2}k_2 + \frac{1}{2}k_3$ and $\kappa_2 = \frac{1}{2}\sqrt{(k_1^2 + 2k_1 k_2 - 2k_1 k_3 + k_2^2 + 2k_3 k_2 + k_3^2)}$,